

Supporting Information

Unraveling the Intricacies of Residual Lithium in High-Ni Cathodes for Lithium-ion Batteries

*Youngjin Kim, Hyoju Park, Jamie H. Warner and Arumugam Manthiram**

Department of Mechanical Engineering and Texas Materials Institute,

The University of Texas at Austin, Austin, Texas 78712, USA.

AUTHOR INFORMATION

Corresponding Author

* Phone: (512) 471-1791; E-mail: manth@austin.utexas.edu

Table of contents

Experimental Section	3
Supplementary Note 1 (Effect of Li_2CO_3 impurity in lithium raw materials)	6
Supplementary Note 2 (Investigation of interdiffusion with TEM)	11
Supplementary Note 3 (Cell fading mechanism)	14
Figure S7 Morphologies	16
Figure S8 Refined powder diffraction patterns	17
Figure S9 Titration curves of 0.025 M LiOH analytes	18
Table S1 Refined cell parameters and statistics obtained from the Rietveld refinement	19
References	20

Experimental Section

Materials Synthesis: The $\text{Ni}_{0.91}\text{Mn}_{0.03}\text{Co}_{0.06}(\text{OH})_2$ precursors were synthesized by a hydroxide co-precipitation method with a continuously stirred tank reactor (CSTR). Sulfate precursors of Ni, Co, and Mn (Ni:Co:Mn = 91:6:3 molar ratio) were dissolved in deionized water and stirred to achieve a homogeneous solution. The concentrations of Ni, Co, and Mn in the aqueous solution mixture were 1.0 M. Then, a stoichiometric amount of ammonium hydroxide (NH_4OH) and sodium hydroxide (NaOH) solutions were continuously fed while stirring to form co-precipitated $\text{Ni}_{0.91}\text{Mn}_{0.03}\text{Co}_{0.06}(\text{OH})_2$. The precursor was thoroughly washed with distilled water, filtered several times, and dried overnight at 180 °C. The as-prepared precursors were then thoroughly mixed with lithium raw materials, including lithium hydroxide monohydrate (Alfa Aesar, Battery grade) and anhydrous lithium hydroxide (Alfa Aesar, 98%) after different storage periods. The lithium hydroxide monohydrate and anhydrous lithium hydroxide were, respectively, stored in air and in an inert glovebox for 1, 60, and 180 day(s). Then, the mixtures were heated under O_2 atmosphere at 670 °C for 10 h (heating and cooling rates: 2 °C min^{-1}). Also, cathode materials with high Li_2CO_3 contents were synthesized with a mixed lithium raw material containing LiOH and Li_2CO_3 (molar ratio = 8:1). For dry cobalt hydroxide coating, the as-prepared $\text{LiNi}_{0.91}\text{Mn}_{0.03}\text{Co}_{0.06}\text{O}_2$ (10 g) was physically mixed with 0.04 M cobalt hydroxide (0.4g, Alfa Aesar, 97%). Then, the mixture was calcined at 720 °C for 6 h in pure O_2 stream.

Characterization: The morphologies of the samples were examined with a SEM (FEI Quanta 650). XRD patterns were obtained with a Rigaku Miniflex 600 equipped with $\text{Cu K}\alpha$ radiation from a 2θ range of 10° to 80° with a step scan of 0.04°. Fullprof program was utilized to perform the Rietveld refinement. Cross-sections of the cathode particles were obtained with focused ion beam (FIB, Scios 2HiVac Dual beam FIB, Thermo Fisher Scientific). Structural

and chemical analyses were performed with a HR-STEM (NEOARM Low kV STEM Corrected, JEOL). Electrochemical impedance spectroscopy (EIS) of hyd-NMC91 and Co-hyd-NMC91 after the formation cycle and 100 cycles at 3 V *versus* Li was performed with a Biologic VMP3 potentiostat. The frequency was scanned between 1 mHz and 1 MHz. To determine the reaction temperature during synthesis, thermogravimetric-differential thermal analysis (TG-DTA) was performed with a NETZSCH STA 449 Jupiter thermal analysis system. The mixtures were heated in an alumina crucible in air (N₂:O₂ = 80:20) from 30 to 800 °C with a 5 °C min⁻¹ heating rate. The residual lithium content in each sample was determined with an acid-base titration. 2 g of sample was put into 100 mL of deionized water or anhydrous methanol (99.9%, Alfa Aesar) for 10 min and then filtered to collect a clear solution. Storage and preparation of the analyte in methanol solvent was performed in an inert glove box. In case of filtered methanol solution, more water was added (methanol/water ratio of 2/3) to minimize the pH error.¹ Afterward, the filtered mixture was titrated with 0.1 M HCl (Easy pH, Mettler Toledo) down to pH 3, and the residual lithium contents as well as individual LiOH and Li₂CO₃ contents were determined by 2-equivalence points. The residual lithium contents of all the samples were determined within 10 minutes after synthesis to minimize the formation of residual lithium in contact with air. A more detailed calculation equations for residual lithium concentration and contents were reported by our group.² 2 g (W) of cathode material was added to 100 ml (A₁) of de-ionized water in a sealed container and then stirred for 10 minutes. The resulting solution was filtered, and then 80 ml (A₂) of the filtered analyte was titrated with 0.01 M (C_{HCl}) HCl standard solution. The residual lithium concentration was calculated with the obtained two equivalence points (V₁ and V₂ in the order of appearance, both in ml) by the formula below:

1) Total residual lithium concentration (ppm) =

$$V_2 \times C_{HCl} \times M_{Li} \times \frac{1}{W} \times \left(\frac{A_1}{A_2}\right) \times 1000 \text{ (ppm)}$$

2) LiOH and Li₂CO₃ content (wt. %)

$$\text{LiOH (wt. \%)} = \left[\frac{(2V_1 - V_2) \times C_{HCl} \times M_{LiOH}}{1000 \times W} \right] \times \left(\frac{A_1}{A_2}\right) \times 100 \text{ (wt. \%)}$$

$$\text{Li}_2\text{CO}_3 \text{ (wt. \%)} = \left[\frac{(V_2 - V_1) \times C_{HCl} \times M_{Li_2CO_3}}{1000 \times W} \right] \times \left(\frac{A_1}{A_2}\right) \times 100 \text{ (wt. \%)}$$

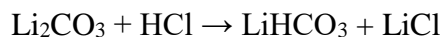
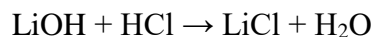
* M_{Li}: 6.941, M_{LiOH}: 23.94, and M_{Li₂CO₃}: 73.89

Electrochemical Tests: A typical cathode slurry was prepared by mixing the electrode material, carbon black (Super P), and poly(vinylidene fluoride) (PVdF) (weight ratio = 90:5:5) in *N*-methyl-2-pyrrolidone (NMP). The slurry was casted onto an Al current collector and the mass loading was ~ 5 mg cm⁻². Galvanostatic tests were carried out with 2032 coin cells assembled with a Li metal anode, an electrolyte consisting of 1.0 M LiPF₆ in ethylene carbonate (EC)/ethyl methyl carbonate (EMC) (weight ratio = 3:7) with 2 wt. % vinylene carbonate (VC) additive, and the prepared cathode at 30 °C. For the formation cycle, all the cathodes were cycled between 3 and 4.35 V (vs. Li/Li⁺) at C/10 rate for 3 cycles, followed by 100 cycles at C/2 rate between 3 and 4.3 V (vs. Li/Li⁺) with a constant current–constant voltage charging mode (cut-off when the current equivalent to C/20 is reached).

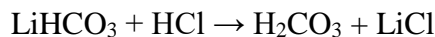
Supplementary Note 1 (Effect of Li₂CO₃ impurity in lithium raw materials)

Lithium hydroxide monohydrate (LiOH•H₂O) is widely used as a lithium raw material for the synthesis of high-Ni layered oxides due to its higher activity at the relatively low synthesis temperatures than Li₂CO₃.³⁻⁷ Recently, Dahn's group reported that generation of (003) peak and (10-8)/(110) peaks shift were observed at ~ 575 °C (LiOH) and 775 °C (Li₂CO₃) during the synthesis of LiNiO₂ with different lithium raw materials.⁴ Furthermore, an endothermic peak near 721 °C as a result of fusion of Li₂CO₃ was clearly observed in the differential scanning calorimetry (DSC) analysis from the mixture of Li₂CO₃ and Ni(OH)₂,⁵ indicating that Li₂CO₃ is still remaining at the melting point. Both phenomena revealed that a higher temperature is required to prepare fully lithiated high-nickel cathode materials when using Li₂CO₃ as the lithium source, instead of LiOH. Moreover, the surface of lithium hydroxide is gradually converted to lithium carbonate when lithium hydroxide is stored in air,⁸⁻¹⁰ which is thermodynamically favorable ($\Delta G < 0$). Therefore, 670 °C is not high enough for Li₂CO₃ impurity in the lithium raw materials to react with NMC91 precursors completely to form high-nickel NMC cathode materials (Ni contents: 91%).

Titration of anhydrous lithium hydroxide with different storage time in air can provide the evidence for the formation of Li₂CO₃. Three anhydrous LiOH powder samples were stored in air for 0 (anh-0), 10 (anh-10), and 20 (anh-20) days and their temperature and relative humidity for 20 days are shown in **Figure S1a**. To enhance the reaction rate, anhydrous lithium hydroxide was finely ground inside a glovebox. **Figure S1b** shows the titration curves of the three samples. Two equivalence points can be determined in the mixed solution of LiOH and Li₂CO₃ with differences in their base strengths when the titrant is an acid (*e.g.* 0.1 M HCl).² The first equivalent point EP (EP₁) is a combination of two EPs corresponding the two reactions below:



EP₂ corresponds to the reaction below:



Difference in the volume between EP₂ and EP₁ (EP₂ – EP₁) reflects the conversion amount of LiOH to Li₂CO₃, as shown in **Figure S1c**. The anh-0 showed only EP₁, which means Li₂CO₃ impurity in anhydrous lithium hydroxide is extremely low. On the other hand, two equivalence points of anh-10 and anh-20 are clearly observed and the volume of (EP₂ – EP₁) is significantly increased with increasing storage periods. This indicates that Li₂CO₃ is gradually formed in anhydrous LiOH and its content is increased with storage time during the storage of anhydrous LiOH in air.

To demonstrate the effect of lithium carbonate impurity in the lithium raw materials during synthesis of NMC91 without inaccuracy issues introduced by Li₂CO₃ impurity, we prepared a mixture of anhydrous lithium hydroxide and Ni_{0.91}Mn_{0.03}Co_{0.06}(OH)₂ precursors to synthesize anh-NMC91. The mixture was then stored in air for different storage times and fired at the same condition. To avoid off-stoichiometry issues, all the mixtures of anhydrous lithium and NMC precursors were prepared inside the glovebox. The anhydrous lithium hydroxide and NMC precursors were thoroughly mixed in the molar ratio of 1.00 (anh-NMC91). A part of those mixtures was stored in air for 10 (anh-NMC91-10) and 20 days (anh-NMC91-20). After that, each mixture was fired at 670 °C for 10 hr in a pure stream of oxygen and titrated with an auto-titrator. **Figure S1d** exhibits the residual lithium content in the as-prepared three cathode materials. The Li₂CO₃ content is significantly increased with increasing storage period in air (anh-NMC91 < anh-NMC91-10 < anh-NMC91-20). This is attributed to the fact that Li₂CO₃ impurity is gradually formed in anhydrous lithium hydroxide during air storage (**Figure S1c**),

resulting in an accumulation of Li_2CO_3 on the surface after the synthesis of NMC91 cathode materials.

We further investigated the anhydrous LiOH and Li_2CO_3 mixture as a lithium source for NMC91 synthesis to verify the melting point effect of lithium raw materials. It is well known that $\text{LiOH-Li}_2\text{CO}_3$ eutectic molten salt melting point can be significantly reduced ($433\text{ }^\circ\text{C}$) based on the phase diagram theory.¹¹⁻¹³ Two NMC91 cathode materials with two different lithium source mixtures ($\text{LiOH-Li}_2\text{CO}_3$ ratio: 0.84:0.16 and 0.92:0.08) were prepared, as referred to CO3-NMC91-16 and CO3-NMC91-08. To avoid off-stoichiometry issues, all mixtures were prepared inside the glovebox (Li/TM ratio: 1.00). **Figure S1e** and **f** show the residual lithium contents and XRD of anh-NMC91, CO3-NMC91-16 and CO3-NMC91-08. With increasing Li_2CO_3 molar ratio in the binary salt mixture, Li_2CO_3 content significantly increased while the $I_{(003)}/I_{(104)}$ ratio decreased. TG-DTA results revealed insufficient reaction of Li_2CO_3 during NMC91 synthesis. The TG-DTA curves of the mixture of $\text{Ni}_{0.91}\text{Mn}_{0.03}\text{Co}_{0.06}(\text{OH})_2$ with molten Li salt ($[(1-x)\text{LiOH}\cdot\text{H}_2\text{O} - x\text{Li}_2\text{CO}_3]$ with $x = 0.16$) and anhydrous LiOH are shown in **Figure S1g** and **h**. When the Li source is a molten salt, an endothermic peak of Li_2CO_3 ($721\text{ }^\circ\text{C}$) was clearly observed.⁵ On the other hand, there were no peaks near $721\text{ }^\circ\text{C}$ when using anhydrous LiOH . Moreover, the melting point of eutectic molten salt ($422\text{ }^\circ\text{C}$) was lower than anhydrous LiOH ($463\text{ }^\circ\text{C}$). This means that LiOH and Li_2CO_3 in the molten salt were separately reacted with NMC hydroxide precursors during synthesis despite lower melting point as well as Li_2CO_3 is not enough to fully react at the synthesis temperature of NMC91 ($670\text{ }^\circ\text{C}$). Consequently, the formation of inferior structure ($I_{(003)}/I_{(104)} < 1.2$) and high Li_2CO_3 content on high-nickel cathode materials were observed when using Li_2CO_3 as the lithium source, as shown in **Figure S1e** and **f**.

Based on these results, the possible formation mechanisms of Li_2CO_3 on the surface of high-Ni cathodes are proposed. (1) Unreactive Li_2CO_3 due to insufficient reaction at the synthesis

temperature can be accumulated, which is further supported by **Figure S1**. (2) Residual lithium in high-Ni layered oxide cathodes can be formed when exposed to air. Surface Li_2O and/or LiOH are converted to Li_2CO_3 . This reaction is not only thermodynamically favorable ($\Delta G < 0$) but also one of the formation mechanisms of residual lithium. (3) Additional Li_2CO_3 on high-Ni cathodes could be formed during cooling.¹⁴

Therefore, lithium raw materials for the synthesis of high-Ni cathode materials should be stored in a moisture and/or CO_2 controlled environment to avoid Li_2CO_3 impurity issue.

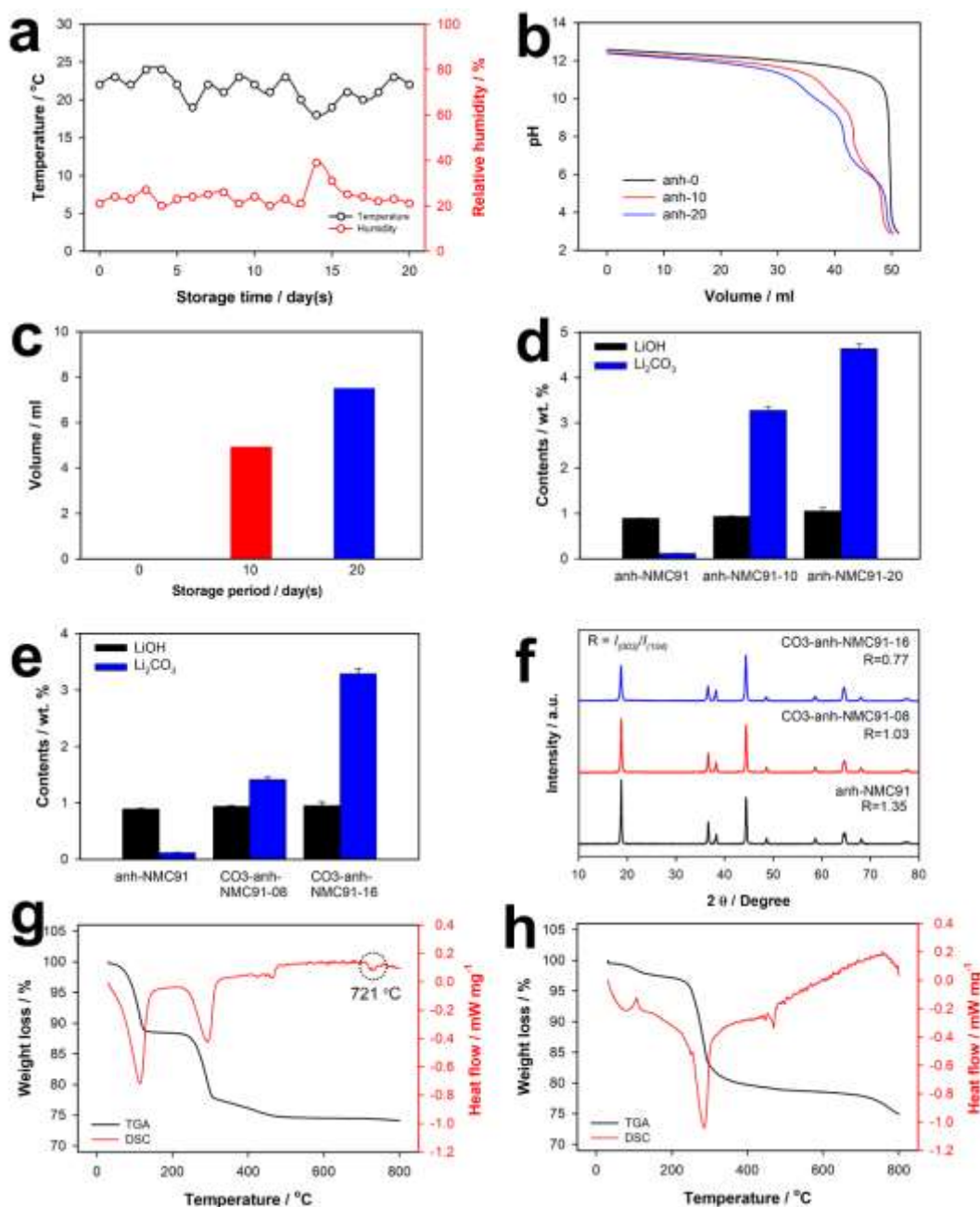


Figure S1. (a) Temperature and relative humidity in the lab for 20 days, (b) titration curves and (c) difference between the EP₂ and EP₁ values for the anh-0, anh-10, and anh-20 samples, (d) residual lithium contents in mixture of anhydrous LiOH and NMC91 precursors in air with increasing storage time, (e) residual lithium contents and (f) XRD patterns of NMC91 with mixed LiOH anhydrous and Li₂CO₃ ($[(1-x)\text{LiOH} : x\text{Li}_2\text{CO}_3]$, molar ratio of $x = 0, 0.08,$ and 0.16), and TG-DTA curves of Ni_{0.91}Mn_{0.03}Co_{0.06}(OH)₂ with (g) mixed Li salt ($[(1-x)\text{LiOH}\cdot\text{H}_2\text{O} - x\text{Li}_2\text{CO}_3]$ with $x = 0.16$) and (h) anhydrous LiOH.

Supplementary Note 2 (Investigation of interdiffusion with TEM)

Figure S2a shows the cross-sectional image of Co-hyd-NMC91. As shown, nanostructured materials (~ 200 nm) are on the surface of NMC91. To further determine the fine structure of the nanostructured coating materials, high-angle annular dark-field STEM (HAADF-STEM) imaging and electron energy loss spectroscopy (EELS) were conducted, as shown in **Figure S2b** and **d**. The well-defined layered structure of the corresponding red box in Figure S2a is clearly observed as a stacking of each transition-metal layer along the *c*-axis (Figure S2b), which is consistent with the primary particle of Co-hyd-NMC91 (blue box in Figure S2a) shown in **Figure S2c**. This structure consists of Co, Ni and O, and the composition is revealed to be $\text{LiCo}_x\text{Ni}_{1-x}\text{O}_2$ by the EEL spectra (**Figure S2d**). This indicates that transition-metal ions between the coating layer and the bulk are cross-diffused.¹⁵⁻¹⁷ Lithium cobalt oxides, such as layered LiCoO_2 and lithium deficient spinel Li_xCoO_2 , can be formed by a reaction between residual lithium and cobalt hydroxide.¹⁸ Hence, $\text{LiCo}_x\text{Ni}_{1-x}\text{O}_2$ is additionally formed from interdiffusion between lithium cobalt oxide and hyd-NMC91 on the surface where both particles are adjacent to each other. This interdiffusion can be observed in cobalt coated-anh NMC91, as shown in **Figure S3**. Co-rich (78%) and Ni-poor (21%) concentration are also clearly observed in the middle of the nanostructured material that is adjacent to the primary particles of NMC91 (Figure S4).

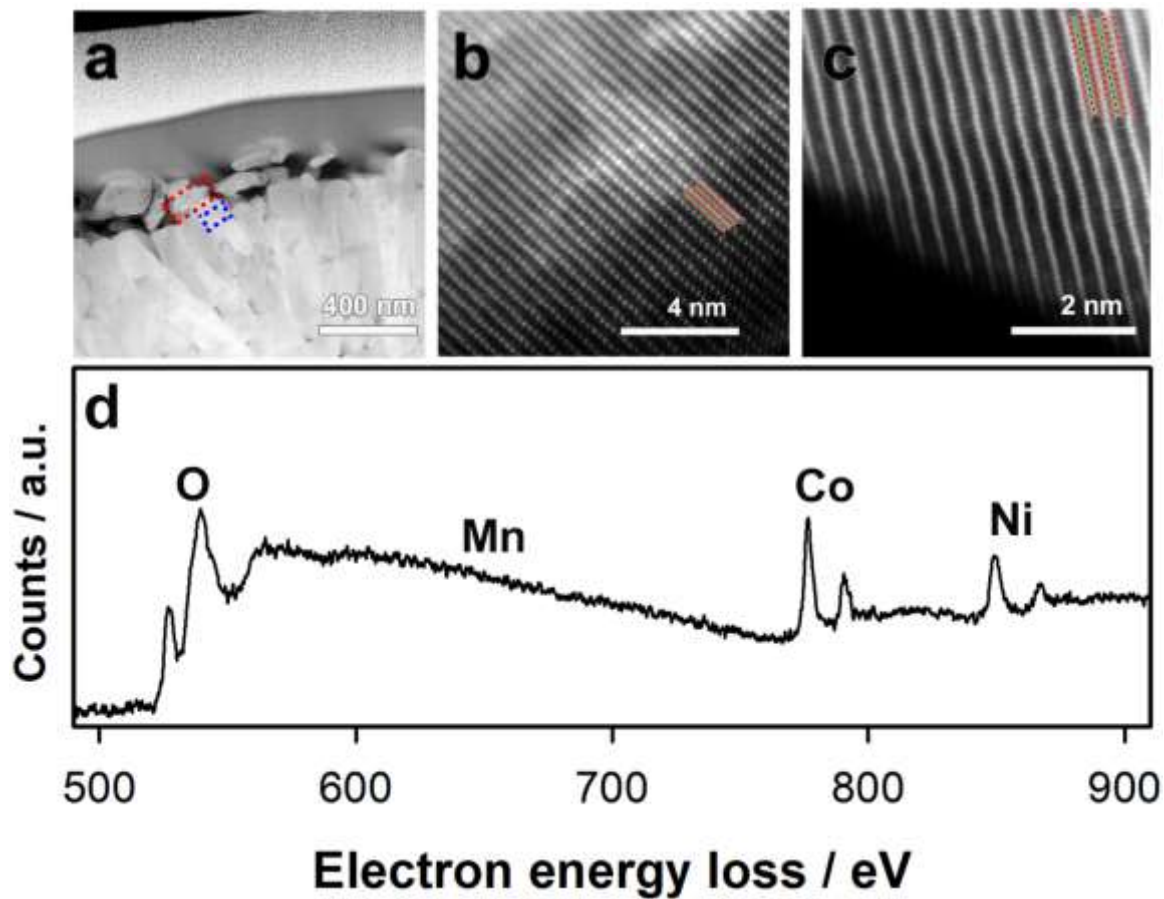


Figure S2. TEM analysis. (a) Cross-sectional image of the Co-hyd-NMC91 particle from STEM, showing ~ 200 nm sized nanostructured coating material distributed on the surface of the NMC91 particle (typical coating material marked with the red box) and primary particles of Co-hyd-NMC91 (typical primary particle marked with the blue box). HAADF-STEM image of the coating material (red box in (a)) on the (b) surface and (c) bulk of Co-hyd-NMC91, showing the layered structure (red: oxygen, gray: transition metal, and green: lithium). (d) EEL spectrum revealing that the coating material is the layered $\text{LiNi}_x\text{Co}_{1-x}\text{O}_2$.

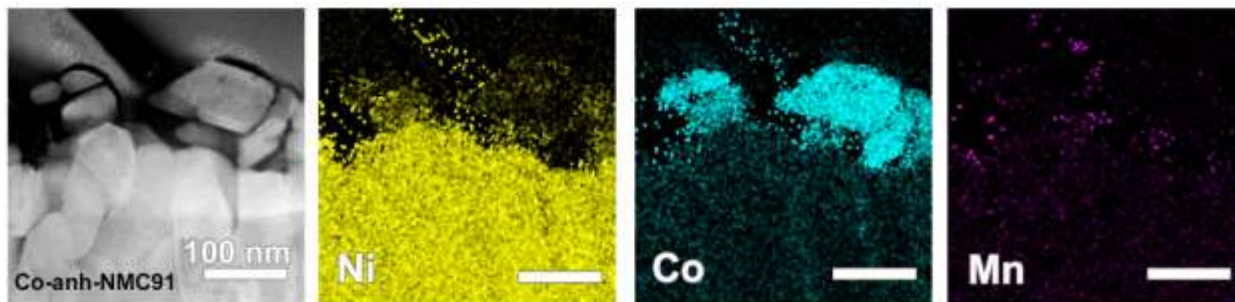


Figure S3. HR-TEM image and corresponding EDS elemental maps of Ni (yellow), Co (cyan), and Mn (purple) in Co-anh-NMC91. All scale bars represent 100 nm.

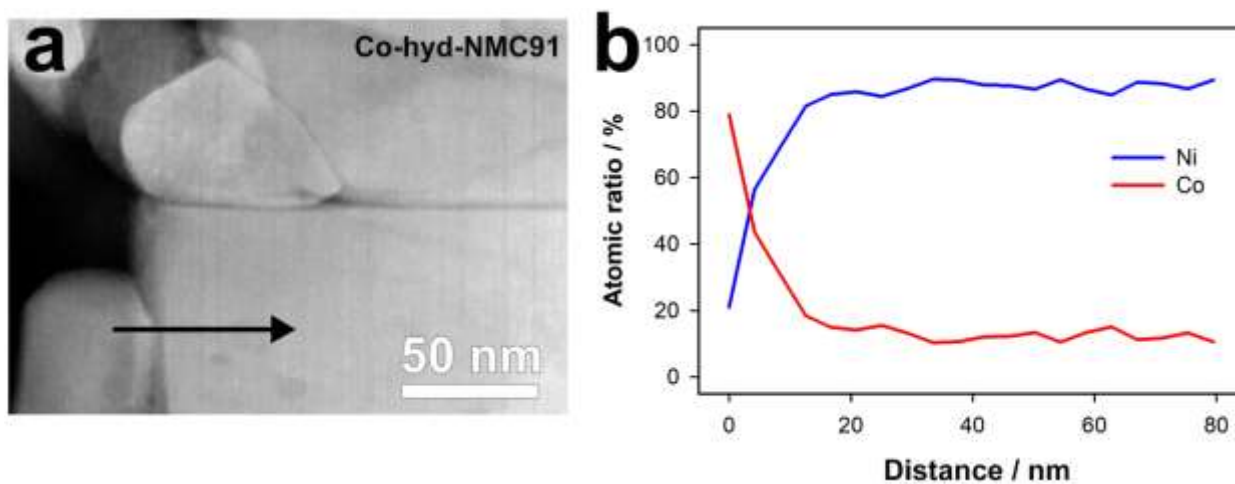


Figure S4. Interdiffusion of Co and Ni ions in Co-hyd-NMC91: (a) HR-TEM image of Co-hyd-NMC91 and (b) EDS line scans of Ni (blue) and Co (red) distribution along the black arrow (~80 nm).

Supplementary Note 3 (Cell fading mechanism)

The phase transition from hexagonal (H1) to monoclinic (M), monoclinic (M) to hexagonal (H2), and hexagonal (H2) to hexagonal (H3) are clearly observed during the charge and discharge process.^{3, 19-21} Notably, the H2-H3 phase transition causes the 'c' axis to drastically contract, resulting in microcrack. Cobalt hydroxide coated NMC91 showed a lower intensity of the H2 – H3 phase transition peak than the uncoated NMC91 electrodes, which has contributed to the improvement in cycle performance. Therefore, the intensity and reversibility of the peaks corresponding to the H2 to H3 phase transition are critical indicators for the structural stability of high Ni-cathodes.

To verify the microcrack after longterm cycling, morphologies of hyd-NMC91 and Co-NMC91 after 100 cycles were examined with SEM (**Figure S5**). The microcrack of hyd-NMC91 (**Figure S5a and b**) is clearly observed compared to that in Co-hyd-NMC91 (**Figure S5c and d**) in the cross-sectional images. Relatively bright particles (white circles) in low magnitude images indicate cracked particles. The hyd-NMC91 has more brighter particle region than Co-hyd-NMC91, illustrating a more widespread cracking (**Figure S5e**). Moreover, the impedance growth of hyd-NMC91 and Co-hyd-NMC91 after 100 cycles was observed with EIS (**Figure S6**). It is clear that the overall impedance growth of Co-hyd-NMC91 is substantially lower than that of hyd-NMC91 after cycling. There is little difference in the surface cathode-electrolyte interphase (CEI) and charge-transfer resistance after the formation cycles. However, the CEI resistance of hyd-NMC91 (194 Ω) after 100 cycles is about three times higher than that of Co-hyd-NMC91 (66 Ω), as shown in **Figure S6c**. This means that additional electrolyte decomposition could be effectively reduced after cobalt hydroxide coating in NMC91 due to the removal of residual lithium and decreasing microcrack. Therefore, cobalt-coating on high nickel cathode materials contributes to less CEI resistance growth, resulting in improvement in cycle performance.

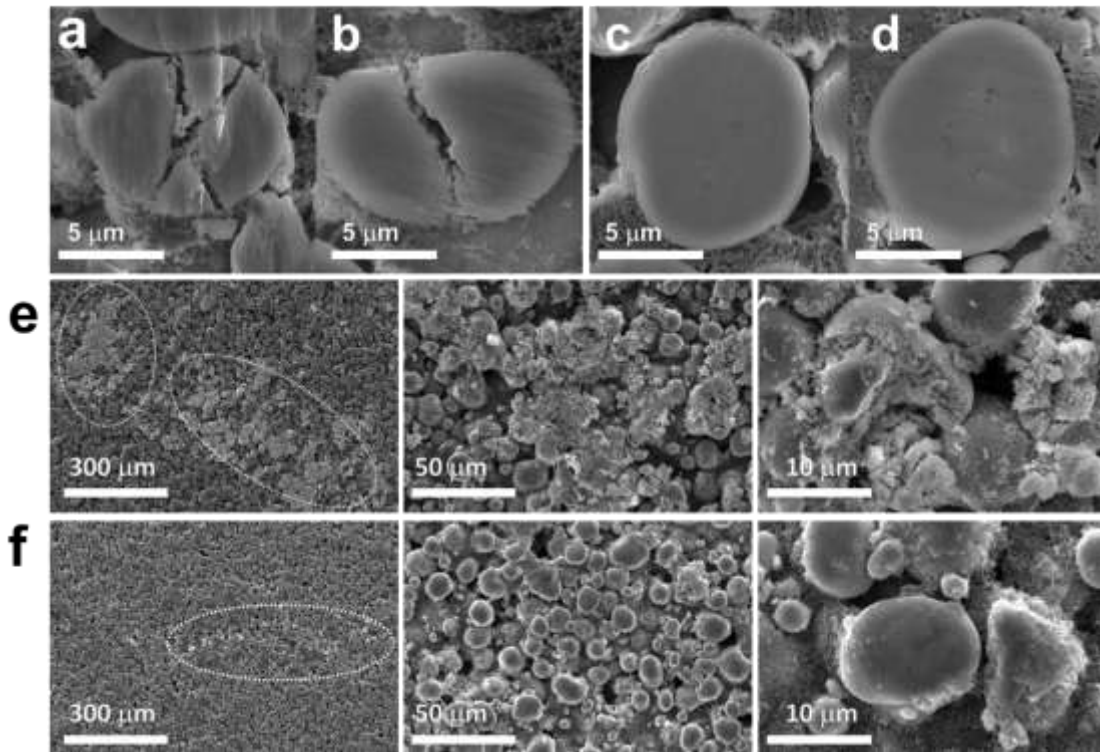


Figure S5. Cross-sectional SEM images of (a), (b) hyd-NMC91 and (c), (d) Co-hyd-NMC91 and SEM images at various magnifications (x200, x2000, and x4000) of (e) hyd-NMC91 and (f) Co-hyd-NMC91 after 100 cycles. The white circles highlight the cracked particles.

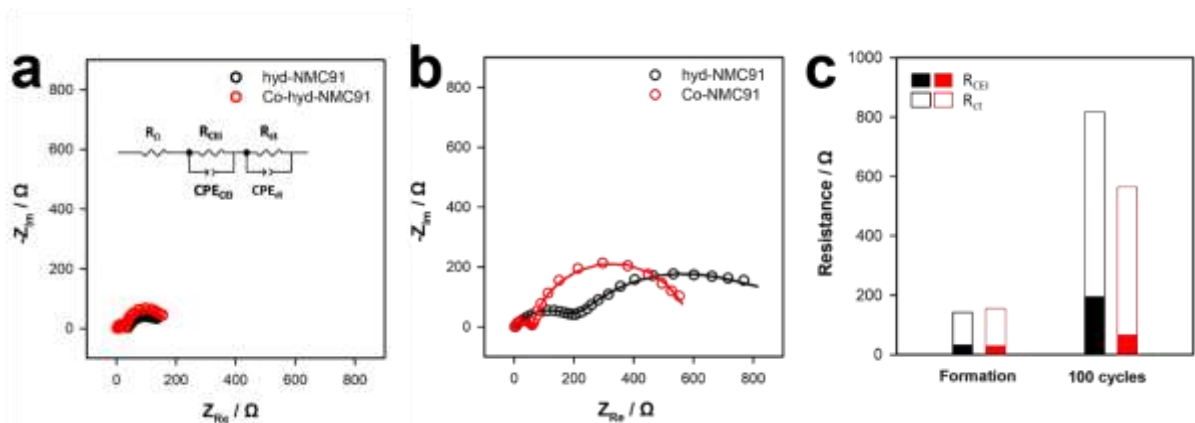


Figure S6. Electrochemical impedance spectroscopy of hyd-NMC91 and Co-hyd-NMC91 (a) after the formation cycle (the inset shows the equivalent circuit) and (b) 100 cycles; (c) CEI resistance and charge-transfer resistance of hyd-NMC91 (black) and Co-hyd-NMC91 (red) after the formation cycle and 100 cycles.

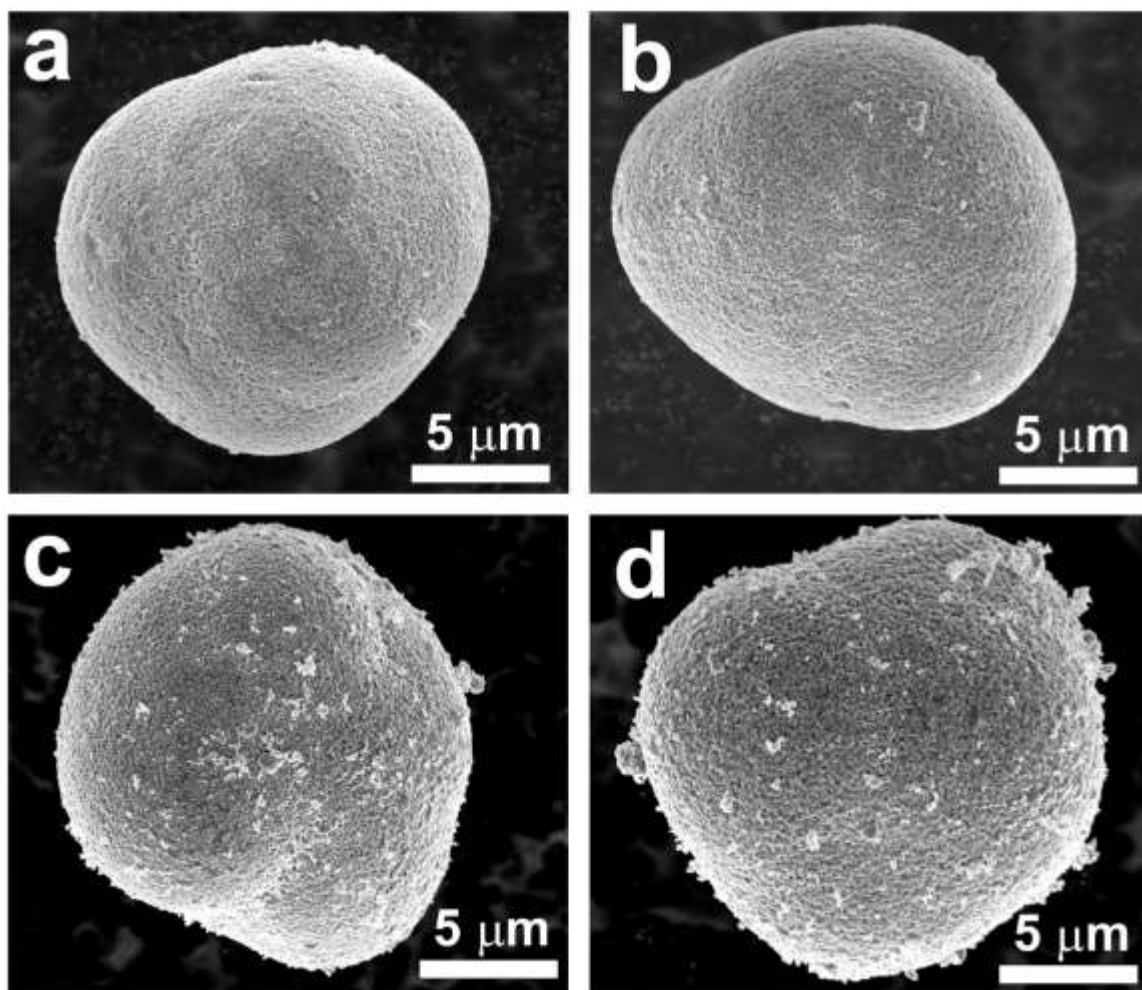


Figure S7. Morphologies of (a) hyd-NMC91, (b) anh-NMC91, (c) Co-hyd-NMC91, and (d) Co-anh-NMC91.

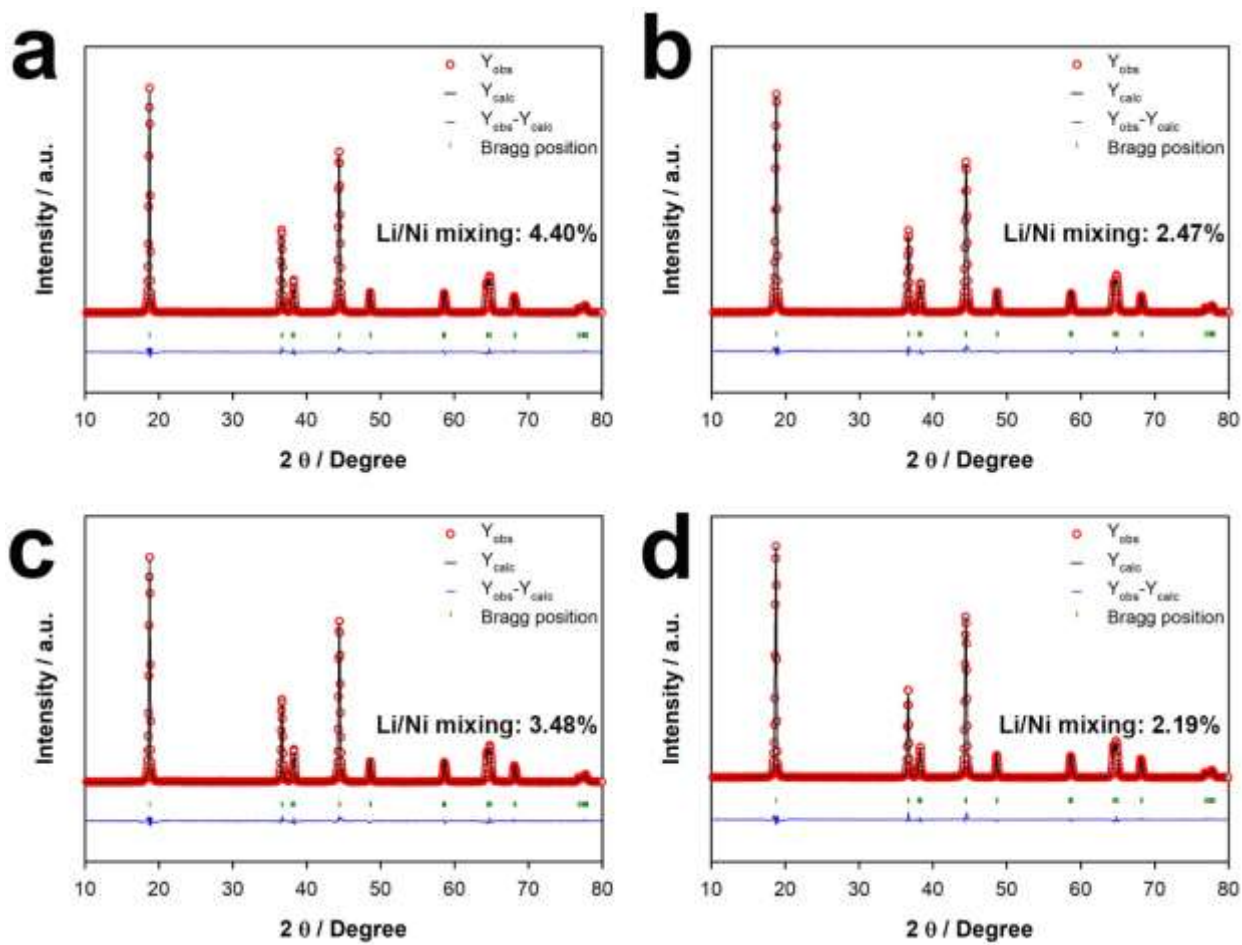


Figure S8. Refined powder diffraction patterns of (a) hyd-NMC91, (b) anh-NMC91, (c) Co-hyd-NMC91, and (d) Co-anh-NMC91.

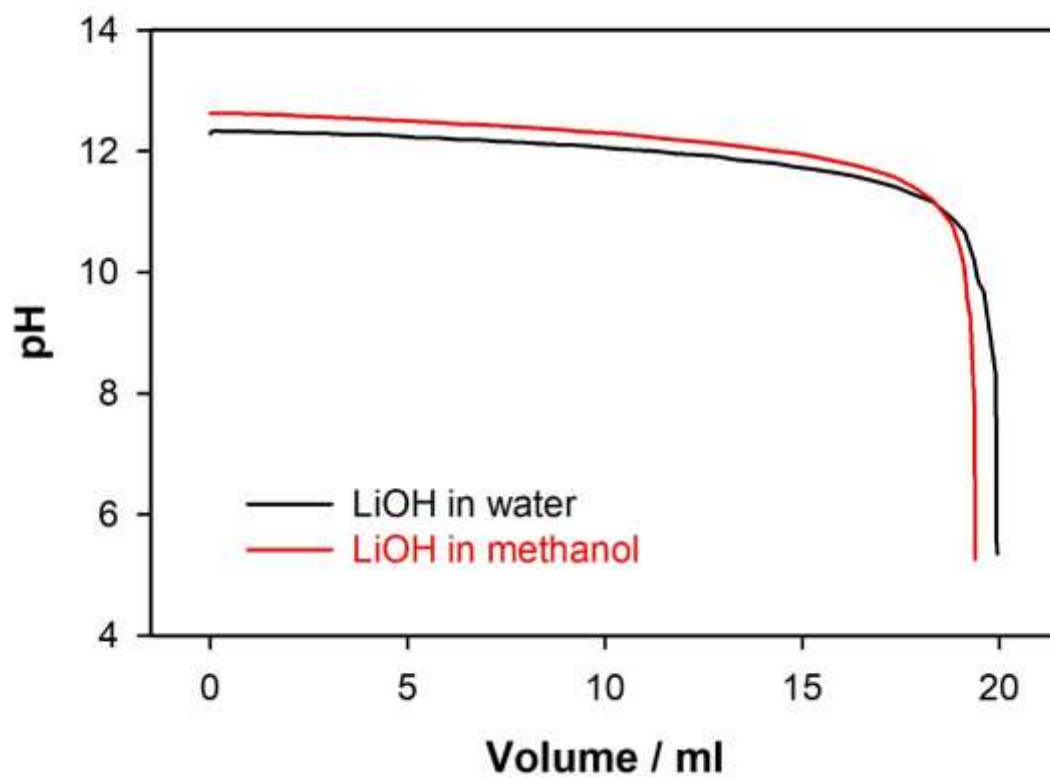


Figure S9. Titration curves of 0.025 M LiOH analytes prepared with water (black) and methanol (red) as solvents.

Table S1 Refined cell parameters and statistics obtained from the Rietveld refinement of the powder XRD patterns of hyd-NMC91, anh-NMC91, Co-hyd-NMC91, and Co-anh-NMC91

Parameter	hyd-NMC91	anh-NMC91	Co-hyd-NMC91	Co-anh-NMC91
a-axis (Å)	2.87597	2.87427	2.87540	2.87423
c-axis (Å)	14.19703	14.19796	14.19677	14.19781
Volume (Å ³)	101.695	101.581	101.652	101.573
Ni ²⁺ in Li site (%)	4.40	2.47	3.48	2.19
R _p (%)	4.02	4.38	4.63	4.29
R _{wp} (%)	5.73	6.03	6.58	5.91
χ^2	5.22	6.09	7.49	6.17

References

- (1) Kotrba, M.; Schilling, L.-H., Measurement of pH in Ethanol, Distilled Water, and their Mixtures: On the Assessment of pH in Ethanol-Based Natural History Wet Collections and the Detrimental Aspects of Dilution with Distilled Water. *Collect. Forum* **2017**, *31* (1-2), 84-101.
- (2) Seong, W. M.; Kim, Y.; Manthiram, A., Impact of Residual Lithium on the Adoption of High-Nickel Layered Oxide Cathodes for Lithium-Ion Batteries. *Chem. Mater.* **2020**, *32* (22), 9479-9489.
- (3) Ohzuku, T.; Ueda, A.; Nagayama, M., Electrochemistry and Structural Chemistry of LiNiO₂ (R3m) for 4 Volt Secondary Lithium Cells. *J. Electrochem. Soc.* **1993**, *140* (7), 1862-1870.
- (4) Weber, R.; Li, H.; Chen, W.; Kim, C.-Y.; Plucknett, K.; Dahn, J. R., In Situ XRD Studies During Synthesis of Single-Crystal LiNiO₂, LiNi_{0.975}Mg_{0.025}O₂, and LiNi_{0.95}Al_{0.05}O₂ Cathode Materials. *J. Electrochem. Soc.* **2020**, *167* (10), 100501.
- (5) Deng, S.; Xue, L.; Li, Y.; Lin, Z.; Li, W.; Chen, Y.; Lei, T.; Zhu, J.; Zhang, J., Structural Evolution and Formation Mechanism of LiNiO₂ During High-Temperature Solid-State Synthesis. *J. Electrochem. En. Conv. Stor* **2019**, *16* (3), 031004
- (6) Kim, B.; Kim, J.; Song, M.; Ida, T.; Ishizawa, N. In *The effect of oxygen pressure on the synthesis of LiNiO₂*, Solid State Phenomena, Trans Tech Publ: 2007; pp 1043-1046.
- (7) LIN, S.-P.; Fung, K.-Z.; HON, Y.-M.; HON, M.-H., Reaction mechanism of LiNiO₂ synthesized in oxygen atmosphere by Pechini method. *J. Ceram. Soc. Jpn.* **2002**, *110* (1288), 1038-1043.
- (8) Yi, W. t.; Yan, C. y.; Ma, P. h.; Li, F. q.; Wen, X. m., Refining of crude Li₂CO₃ via slurry phase dissolution using CO₂. *Sep. Purif. Technol.* **2007**, *56* (3), 241-248.
- (9) Williams, D. D.; Miller, R. R., Effect of Water Vapor on the LiOH-CO₂ Reaction. Dynamic Isothermal System. *Ind. Eng. Chem. Fundamen.* **1970**, *9* (3), 454-457.
- (10) Zhuo, Z.; Fu, P.; Zhao, B. In *Studies on Reaction Kinetics of LiOH for Absorbing CO₂*, 2009 Asia-Pacific Power and Energy Engineering Conference, 27-31 March 2009; 2009; pp 1-4.
- (11) Jiang, G.; Zhang, Y.; Meng, Q.; Zhang, Y.; Dong, P.; Zhang, M.; Yang, X., Direct Regeneration of LiNi_{0.5}Co_{0.2}Mn_{0.3}O₂ Cathode from Spent Lithium-Ion Batteries by the Molten Salts Method. *ACS Sustainable Chem. Eng.* **2020**, *8* (49), 18138-18147.
- (12) Yang, J.; Wang, W.; Yang, H.; Wang, D., One-pot compositional and structural regeneration of degraded LiCoO₂ for directly reusing it as a high-performance lithium-ion battery cathode. *Green Chem.* **2020**, *22* (19), 6489-6496.
- (13) Zhu, H.; Li, J.; Chen, Z.; Li, Q.; Xie, T.; Li, L.; Lai, Y., Molten salt synthesis and electrochemical properties of LiNi_{1/3}Co_{1/3}Mn_{1/3}O₂ cathode materials. *Synth. Met.* **2014**, *187*, 123-129.
- (14) Zhang, M.-J.; Hu, X.; Li, M.; Duan, Y.; Yang, L.; Yin, C.; Ge, M.; Xiao, X.; Lee, W.-K.; Ko, J. Y. P.; Amine, K.; Chen, Z.; Zhu, Y.; Dooryhee, E.; Bai, J.; Pan, F.; Wang, F., Cooling Induced Surface Reconstruction during Synthesis of High-Ni Layered Oxides. *Adv. Energy Mater.* **2019**, *9* (43), 1901915.
- (15) Han, B.; Key, B.; Lapidus, S. H.; Garcia, J. C.; Iddir, H.; Vaughey, J. T.; Dogan, F., From Coating to Dopant: How the Transition Metal Composition Affects Alumina Coatings on Ni-Rich Cathodes. *ACS Appl. Mater. Interfaces* **2017**, *9* (47), 41291-41302.
- (16) Li, J.; Doig, R.; Camardese, J.; Plucknett, K.; Dahn, J. R., Measurements of Interdiffusion Coefficients of Transition Metals in Layered Li-Ni-Mn-Co Oxide Core-Shell Materials during Sintering. *Chem. Mater.* **2015**, *27* (22), 7765-7773.

- (17) Zhao, Y.; Li, J.; Dahn, J. R., Interdiffusion of Cations from Metal Oxide Surface Coatings into LiCoO₂ During Sintering. *Chem. Mater.* **2017**, *29* (12), 5239-5248.
- (18) Kim, J.; Ma, H.; Cha, H.; Lee, H.; Sung, J.; Seo, M.; Oh, P.; Park, M.; Cho, J., A Highly Stabilized Nickel-Rich Cathode Material by Nanoscale Epitaxy Control for High-energy Lithium-ion Batteries. *Energy Environ. Sci.* **2018**, *11* (6), 1449-1459.
- (19) de Biasi, L.; Schiele, A.; Roca-Ayats, M.; Garcia, G.; Brezesinski, T.; Hartmann, P.; Janek, J., Phase Transformation Behavior and Stability of LiNiO₂ Cathode Material for Li-Ion Batteries Obtained from In Situ Gas Analysis and Operando X-Ray Diffraction. *ChemSusChem* **2019**, *12* (10), 2240-2250.
- (20) Xu, J.; Hu, E.; Nordlund, D.; Mehta, A.; Ehrlich, S. N.; Yang, X.-Q.; Tong, W., Understanding the Degradation Mechanism of Lithium Nickel Oxide Cathodes for Li-Ion Batteries. *ACS Appl. Mater. Interfaces* **2016**, *8* (46), 31677-31683.
- (21) Yang, X. Q.; Sun, X.; McBreen, J., Structural Changes and Thermal Stability: in situ X-ray Diffraction Studies of a New Cathode Material LiMg_{0.125}Ti_{0.125}Ni_{0.75}O₂. *Electrochem. Commun.* **2000**, *2* (10), 733-737.